Atomic simulation of melting and surface segregation of ternary Fe-Ni-Cr nanoparticles

X. Zhang[a,b], B. Li[a,b,*], H.X. Liu[b,c], G.H. Zhao[b,d], Q.L. Yang[a], X.M. Cheng[a], C.H. Wong[e,*], Y.M. Zhang[e], and C.W.J. Lim[e]

[a] School of Materials Science and Engineering, Wuhan University of Technology, Wuhan 430070, China

[b] Research Center for Materials Genome Engineering, Wuhan University of Technology, Wuhan 430070, China

[c] International School of Materials Science and Engineering, Wuhan University of Technology, Wuhan 430070, China

[d] School of Computer Science and Technology, Wuhan University of Technology, Wuhan 430070, China

[e] Singapore Centre for 3D Printing, School of Mechanical and Aerospace Engineering, Nanyang Technological University, 50 Nanyang Avenue, Singapore 639798, Singapore

[*]Corresponding authors. E-mail: libei@whut.edu.cn, CHWong@ntu.edu.sg

ABSTRACT

Knowledge of thermodynamics of multimetallic nanoparticles is of great importance in prediction and advancing the understanding of synthesis, characterization, and applications of metal nanoparticles. In this work, molecular dynamics simulations were performed to investigate the melting characteristics and behaviors of a ternary Fe-Ni-Cr nanoparticle (19.17 wt.% Cr, 11.72 wt.% Ni, and the rest Fe). It was found that the melting of the nanoparticles starts from the surface and proceeds gradually inwards to the core, indicating a liquid nucleation and growth melting mode. During heating, severe Cr segregation with increasing temperature were observed, and the nano Cr clusters prefer to aggregate mostly at the surface due to lower surface energy and stronger cohesive interactions of Cr atoms than Fe and Ni. Moreover, the melting temperature of the nanoparticles decreases as the particle radius decreases, and there exists a linear relationship between the melting point and the inverse of the radius. This signifies the feasibility of the linear depression effect for the size-dependent melting of Fe-Ni-Cr nanoparticles accompanying surface segregation and aggregation. The findings in this work are believed to provide the atomic scale understanding of mechanisms of melting and surface segregation of ternary Fe-Ni-Cr nanoparticles.

Keywords: Molecular dynamics, alloy nanoparticle, melting behavior, segregation and aggregation.

1. Introduction

Metal nanoparticles exhibit unique thermodynamic, mechanical and electronic properties different from those of the conventional coarse-grained metal powders ascribing to their large surface area to volume ratios. They have drawn wide attention in numerous potential applications such as actuators, catalysis, sensing and imaging, drug delivery, solar cells, and microstructural engineering, etc. [1-9]. For instance, Ag and Au noble metal nanoparticles exhibit high sensitivity, activity, and enhanced optical absorption and scattering making them attractive in catalysis and sensing applications [3]. Bimetallic nanoparticle catalysts such as *M*-Pt, where *M* = Ni, Fe, Co or Pd, offer exceptional catalytic activity based on structural sensitivity and high surface area when compared to their bulk counterparts [9]. In addition, Fe-based nanoparticles with superior magnetization and biocompatibility are frequently used as magnetic drug-targeting carriers for controlled drug release and enhancement agents in magnetic resonance imaging [4]. Since the key to all the applications is related to their small size and inherent nanostructure, knowledge and control of the size, shape, surface composition, and crystalline structure of the metal nanoparticles is of significant importance to understand synthesis, processing, and performance of the metal nanoparticles from both scientific and technical viewpoints.

Recently, considerable efforts have been dedicated to investigate thermodynamics and kinetics of growth and stabilization of nanoparticles under thermal and other stresses. Experimental and theoretical studies have revealed characteristic size-dependent thermo-physical features such as depression of melting and sintering temperatures of the nanoparticles [10-15]. As the particle size decreases beyond a critical value, the melting temperature of the nanoparticle with free surface deviates from that of its corresponding bulk phase. The depression and deviation effect is mainly associated with the excess energy of the large percentage of weakly bound surface atoms that are less constrained in their thermal motion. Moreover, the kinetics and melting mechanisms of the nanoparticles have been investigated using computational techniques [16-22]. Earlier molecular dynamics (MD) simulations of the melting behavior of spherical Au nanoparticles showed that the premelting begins with the outer layer signaling the approach of the melting point, and proceeds inwards toward the core [16]. The thermal behavior of Na nanoclusters was examined using orbital-free density functional MD method [17]. It was revealed that isomers of Na_{142} and Na_{92} (both incomplete 3-shell icosahedrons) would melt in two steps: surface

premelting and homogenous melting involving diffusion of all the atoms across the cluster. On the contrary, only a single transition was observed for perfect 2-shell icosahedron Na_{55}. Moreover, in bimetallic core-shell systems such as Cu-Ni and Pd-Pt nanoparticles, structural changes accompanying the thermal evolution exhibited a characteristic two-stage melting: a dynamical premelting at the surface followed by homogenous melting of the core [18,19]. In particular, Cu/Pd atoms tend to diffuse and segregate to surface distributing on unsaturated edge sites prior to melting due to their lower surface free energy. Another MD simulation of Co-Pt and Co-Au core-shell structured nanoparticles suggested the existence of a strong dependence of the thermal stability on the structure of the core and the element of the shell [20]. It demonstrated a typical two-stage melting for Co-Au nanoparticles, while the Co core and Pt shell were found to melt concurrently.

In contrast to numerous investigation of monometallic and bimetallic nanoparticles [16-24], far less attention has been devoted to understanding the kinetics and melting behaviors of multimetallic nanoparticles. The additional interatomic interactions and coupling could make thermodynamic phenomena, i.e., surface melting and segregation, more complicated. Therefore, in this work, we employ MD simulation method to investigate the dynamic and melting behaviors of ternary Fe-Ni-Cr nanoparticles. The Fe-Ni-Cr alloy model has been chosen as it is the main constituent of a widely used structural alloy, 316L stainless steel. More importantly, microstructural characterization using electron backscatter diffraction (EBSD) and energy dispersive spectroscopy (EDS) has revealed that Cr atoms accumulate around the edges of the cellular structure, signifying Cr diffusion and segregation to the grain boundaries [25]. The distinct interface/surface segregation is of vital importance since it can affect most the physical and chemical properties. It was reported that the Cr segregation deteriorates the magnetic properties of Fe-Cr and Ni-Cr nanoparticles, thereby minimizing their potential applications [26]. However, knowledge and understanding of the mechanisms of Cr segregation in metal nanoparticles is incomplete and limited. In our MD simulations, the melting characteristics and behaviors of the Fe-Ni-Cr nanoparticles will be studied. The physical metallurgical reasons of Cr segregation and aggregation are explored and clarified. Furthermore, the effect of the particle size on the structural evolution and phase transition of the Fe-Ni-Cr nanoparticles during heating will be investigated.

2. Molecular dynamics simulation and methodology

2.1 Molecular models

The Fe-Ni-Cr nanoparticles were initially constructed in a spherical morphology with a face-centered cubic (FCC) crystal structure. All the Fe, Ni, and Cr atoms were distributed stochastically in the lattice sites across the nanoparticles to provide a clear insight on how Cr segregates at different temperatures. Fig. 1 shows a typical equilibrated Fe-Ni-Cr nanoparticle with a radius of R = 60 Å at T = 300 K, signifying a rather smooth surface structure. Clearly, the nanoparticles cannot be perfectly spherical and would, even in their ground state, exhibit some minor facets [16]. To study the effect of the particle size on the melting behavior, we prepared a range of nanoparticles with varying radii from 30 to 70 Å, comprising around 10000 to 126000 atoms. The composition of all the Fe-Ni-Cr nanoparticles was chosen as 19.17 wt.% Cr, 11.72 wt.% Ni, and the remaining to be Fe to mimic a 316L austenitic stainless steel model alloy [25].

2.2 Simulation method

To characterize the interatomic interactions for Fe-Ni-Cr nanoparticles, we adopted an embedded atom method (EAM) potential proposed by Bonny et al. [27]. This potential model has been successfully proven to describe static and dynamic properties of metal alloys containing Fe, Ni and Cr, such as lattice parameters, phase transformation, diffusion coefficient, vacancy forming and dislocation, and thermal conductivity, etc. [28-30]. To verify the applicability of Bonny's EAM potential, we have also simulated the lattice parameter and stacking fault energy for the bulk Fe-Ni-Cr alloys. The simulation results, shown in Table S1, are in good agreement with the experimental data [31-33].

In addition to pair interactions V, the EAM potential contains an embedding energy F dependent on the local electron density ρ. The latter term approximates the many-body contribution from all nearby atoms. The total energy within EAM is thus given as

$$E = \frac{1}{2}\sum_{\substack{i,j=1 \\ j\neq i}}^{N} V_{t_i t_j}(r_{ij}) + \sum_{i=1}^{N} F_{t_i}(\rho_i) \quad (1)$$

where N represents the total number of atoms in the system, r_{ij} is the distance between atoms i and j, and t_i denotes chemical species (Fe, Ni or Cr), respectively. The local electron density around atom i contributed from its neighbors is depicted as

$$\rho_i = \sum_{\substack{j=1 \\ j \neq i}}^{N} \varphi_{t_j}(r_{ij}) \quad (2)$$

where φ denotes the electron density function of the considered element. The details of the parameters of the EAM potential can be found in ref. [27].

Initially, the Fe-Ni-Cr nanoparticles were equilibrated in a cubic simulation box with a side length of 28 nm at T = 300 K for a period of 600 ps. The temperature of the system was maintained constant using the Nose-Hoover thermostat with a relaxation time of 0.2 ps. After equilibration, the nanoparticles were uniformly heated up to 2000 K with a heating rate of 0.25 K/ps, which is compatible with the rates required in laser-related applications [34-39]. The heating duration was 6.8 ns. The Newton's equations of motion were integrated using the Verlet leapfrog algorithm with a time step of 2.0 fs and periodic boundary conditions were applied in all the three dimensions. The MD simulations were carried out using the Large-scale Atomic/Molecular Massively Parallel Simulator (LAMMPS) software [40].

3 Results and discussions

3.1 Structure and shape evolution

The structural features can be expressed through centro-symmetric parameter (CSP) distribution across the nanoparticles. The CSP measures the local lattice disorder around an atom and characterizes whether the atom is part of a perfect lattice, a local defect (e.g., a dislocation or stacking fault), or at a surface. Generally, CSP has a value of zero for a specific perfect lattice and a large non-zero value for thermally disordered or plastically deformed defective systems. Depending on the choice of the reference lattice, the parameter for each atom can be computed as [28,41]

$$\mathrm{CSP} = \sum_{i=1}^{l/2} \left| \boldsymbol{r}_i + \boldsymbol{r}_{i+l/2} \right|^2 \quad (3)$$

where l denotes the number of nearest neighbors for the atom and it has a value of 12 for a FCC lattice, $\boldsymbol{r}_i$ and $\boldsymbol{r}_{i+l/2}$ are the vectors or bonds from the central atom to a particular pairs of opposite nearest neighbors.

Fig. 2 presents the evolution of the CSP values based on the cross-sectional view of the Fe-Ni-Cr nanoparticles. The figure also shows the atomic distribution of the Fe-Ni-Cr nanoparticles with different radii during the heating process. The original FCC structure is chosen as the reference lattice for the CSP calculation such that blue means that the atom belongs to a perfect FCC lattice and red indicates

complete amorphization. It is clearly shown that the nanoparticles exhibit FCC structure and are well equilibrated at T = 300 K before heated up slowly until they totally melt into a liquid phase at high temperatures. As T increases to 1000 K, the nanoparticles could still maintain their spherical crystalline structure. However, they start to melt at about T = 1600 to 1640 K (depending on the particle size) from a very thin liquid layer on the surface, and then proceed gradually inwards to the core, signifying distinct surface melting. This melting process of the Fe-Ni-Cr nanoparticles is also known as the mode of liquid nucleation and growth (LNG) [42-44]. As expected, the surface melting is ascribed to the fact that the surface atoms in finite nanoparticles have more freedom and experience weaker interactions as compared with those in the interior. Moreover, the transition from solid to liquid with increasing temperature undergoes dynamic coexistence melting from the thermodynamic viewpoint. During the melting, the outer liquid-like and inner solid-like atoms could coexist in a particular temperature range between T_{ms} and T_{me}, with T_{ms} being the critical point at which the surface melting starts to occur and T_{me} being the corresponding upper limit point above which liquid state fully develops. Consistent with the literature [42,45], we refer the lower melting limit point T_{ms} as the "melting point" T_m in this work. It is shown in Fig. 2 that, the nanoparticles with smaller radii exhibit decreasing T_m and T_{me}, showing good agreement with experimental and numerical studies [10-15,46]. More importantly, the Cr atoms gradually diffuse, segregate and aggregate to the surface during heating, coinciding well with the EBSD and EDS results for 316L stainless steel [25]. In particular, anomalous "convex nano clusters" are formed, and they even become more intense at higher temperatures in smaller nanoparticles due to the larger surface area to volume ratios. Although bulges and facets began to form at the surface, the nanoparticles could still maintain their spherical shape to some extent. The analysis of the Cr segregation and aggregation will be further discussed in Section 3.3.

3.2 Surface melting and dynamics

Surface melting of nanoparticles refers to the nucleation and propagation of a quasi-liquid layer, which thickens with increasing temperature and ends with the melting of the solid core. Although the surface melting behavior is somewhat revealed in the atomic CSP distribution, better insights into the same phenomenon could be obtained through radial distribution function (RDF) and thermal diffusion.

RDF is an important parameter to describe the structural characteristics of solid, amorphous and

liquid states. It defines the probability of finding an atom in a distance ranging from r to $r + dr$ (dr is the step of calculation) and is expressed as

$$g(r) = \frac{V}{N^2} \frac{\sum_{i=1}^{N_i} n_i(r)}{4\pi r^2 dr} \tag{4}$$

where V and N are the volume and total number of atoms of the system, N_i is the number of atoms around ith atom and $n_i(r)$ is the corresponding atom number in the sphere shell ranging from r to $r +$ dr at the radius r of the nanoparticle, respectively. Fig. 3 shows the total RDFs as functions of the shell radius for the Fe-Ni-Cr nanoparticles at various temperatures corresponding to the critical points in Fig. 2. The first three peaks located at about 2.5, 3.5 and 4.4 Å exemplify the typical FCC crystalline structure at 300 K. The nearest neighbor bond lengths remain almost unaltered (~ 2.5 Å) independent of the radius and temperature, while the major peaks become wider and shallower with increasing temperature. In contrast, the minor peaks appear vaguely at T_m of about 1600 K for R = 40 Å and 1640 K for R = 60 Å, which corresponds to surface melting. After the phase transition is complete, the minor peaks vanish at T_{me} of about 1640 and 1680 K for R = 40 and 60 Å respectively. During the entire melting, the broadening of major peaks and the disappearance of minor peaks of RDFs are characteristic of the solid-to-liquid phase transition of the nanoparticles.

Moreover, the shell-based self-diffusion coefficients (D) are calculated to further investigate the melting mechanism of the Fe-Ni-Cr nanoparticles. By partitioning the particle into several radial shells of equal width dR, the mean square displacement (MSD) calculated within each shell was used to calculate the shell-based self-diffusion coefficients for the atoms in that shell. The width dR was taken as 2.5 Å denoting the nearest neighbor distance between atoms in the Fe-Ni-Cr nanoparticles. The MSDs for each shell and core at different temperatures were obtained by averaging over an atomic trajectory of 20 ps with sampling performed at every 0.02 ps. The shell-based self-diffusion coefficient D was thus obtained from the slope of the MSD curves, which were extracted from the Einstein relation as

$$\langle \Delta r(t)^2 \rangle = \frac{1}{M} \sum_{i=1}^{M} \langle [\boldsymbol{r}_i(t+s) - \boldsymbol{r}_i(s)]^2 \rangle \tag{5}$$

$$D = \lim_{t \to \infty} \frac{1}{6t} \langle \Delta r(t)^2 \rangle \tag{6}$$

where t corresponds to time, $\boldsymbol{r}_i(t+s) - \boldsymbol{r}_i(s)$ is the vector distance of ith atom, the ensemble average is over M atoms and over choices of the time origin s. The value of D at various temperatures and its dependence on the radial distance from the center of the nanoparticles are shown in Fig. 4. To distinguish atomic movement, the shells were divided into three regions and labeled Z_1, Z_2 and Z_3 from the outer to inner regions and the core was labeled Z_4. In all the cases, the diffusivities of the outer shells are higher than those of the inner ones. There is no noticeable atomic movement for any regions in the temperature range of 300 to 1000 K. With further increase in temperature, the inner regions and the core could possess vanishing D exhibiting a typical behavior of a crystalline solid, while the atoms in the outmost region Z_1 begin to move slightly to show a free surface structure. As T reaches the melting point, the D coefficients for the atoms in Z_1 and Z_2 regions gradually increase and the relatively large values indicate the occurrence of the surface melting of the Fe-Ni-Cr nanoparticles. Following that, the atomic mobility in region Z_3 becomes evident and strengthened with temperature due to thermal effect, causing steady growth of the molten liquid layer toward the core. After melting (1640 and 1680 K for R = 40 and 60 Å), the D coefficients increase abruptly and they are almost identical for the inner regions, signifying that the melting of the nanoparticles is complete. It is thus important to note that the melting mechanism of the Fe-Ni-Cr nanoparticles follows the LNG mode and proceeds into two steps. Firstly, the increasing temperature causes higher atomic mobility and a liquid-like layer is formed at the outmost region of the nanoparticle. Then, the molten liquid-like layer thickens with the temperature until the entire nanoparticle including the solid-like core melts.

3.3 Cr segregation and aggregation

At a given composition, surface segregation and aggregation can be determined by both temperature and size of the alloy nanoparticles [26,47-50]. In this work, the temperature- and size-dependent Cr segregation and aggregation in the Fe-Ni-Cr nanoparticles was explored via various characterization techniques including density profile, deformation parameter, and volumetric evolution of Cr aggregates.

Fig. 5 shows the density distribution along the radial direction for the nanoparticles with R = 40 and 60 Å during the heating process. From the total density curves, the solid-like features are preserved at low temperatures (< 1600 K) as is indicated by the distinct numerous peaks. As T increases, the peaks merge and become broader until T_{me}, above which the atomic distribution plateaus, indicative of the

liquid phase. Also, the radial density profiles of Fe, Ni and Cr clearly show the distribution of the three atoms (i.e., Fe, Ni and Cr) with increasing temperature. The Cr atoms begin to diffuse and reside to the surface even at low temperatures, and the surface segregation and protrusion become more severe during the melting process. Contrarily, the Fe and Ni atoms are relatively smoothly distributed across the nanoparticles, and the main constituent Fe atoms compensate the loss of Cr atoms in the specific regions. Noted that the subtle and broad valley-peak pairs are also observed for the Cr atoms inside the particle, signifying the formation of inner Cr aggregates (see the insets of Fig. 5). However, no matter whether the clusters are formed in the interior or at the surface, Cr aggregation is thermally and energetically favored, as is shown in the pair interaction profiles in Fig. 6. The decrease in the pair interaction reveals that the Cr atoms prefer to mix among themselves, and the resulting energy release provides extra energy to assist in melting the nanoparticles. Furthermore, these inner Cr clusters would finally diffuse and coalesce to the surface (see Fig. 7) to reduce the total free energy of the particles.

The deformation parameters are commonly adopted to monitor surface segregation associated with size and shape changes of the nanoparticles. The radial deformation parameter ε_a for each element (a = Fe, Ni or Cr) is expressed as [18,19]

$$\varepsilon_a(t) = \frac{1}{N_a}\sum_{i=1}^{N_a}|\boldsymbol{r}_i(t) - \boldsymbol{r}_{cm}(t)| \tag{7}$$

where N_a is the number of the chosen atoms (Fe, Ni or Cr), and $\boldsymbol{r}_i(t)$ and $\boldsymbol{r}_{cm}(t)$ are the vector positions of ith atom and the nanoparticle center of mass at time t respectively. Fig. 7(a) depicts the variation of ε_a at various temperatures for the nanoparticle with R = 40 Å. Initially, the Cr atoms possessing a smaller $\varepsilon_{\mathrm{Cr}}$ are located closer to the interior as compared to Fe and Ni. As T increases, the deformation parameters increase gradually indicating an outward diffusion of the three atoms in the range of 300 to 1300 K. With further increase in T, the deformation parameter of Cr starts to overweigh that of Fe and $\varepsilon_{\mathrm{Cr}}$ exhibits a larger increasing rate than other two atoms, signifying a stronger temperature-dependent mobility of Cr [27,51]. Then, a sharp increase in $\varepsilon_{\mathrm{Cr}}$ is observed during melting, corresponding to the progressive Cr segregation and aggregation, which is attributed to the lower surface energy of Cr atoms [10]. After melting, inner nano Cr clusters form, however, they prefer to coalesce with adjacent interior clusters to reduce the interfacial free energy. This in turn causes a

sudden decrease in $\varepsilon_{\mathrm{Cr}}$, and the inward diffusion of Cr results in a relatively large single cluster close to the core at 1717 K, as captured in the atomic configuration in Fig. 7(a). $\varepsilon_{\mathrm{Fe}}$ and $\varepsilon_{\mathrm{Ni}}$ show several upward shoulders signifying their outward movement due to the thermal expansion. To further explore the movement of Cr aggregates, the nanoparticles were thermally heated at 2000 K for another 4 ns in an NVT ensemble. The radial deformation parameters were calculated and their time evolution for R = 40 Å is shown in the inset of Fig. 7(a). It is clearly demonstrated that $\varepsilon_{\mathrm{Cr}}$ continues to increase sharply after heating at 2000 K for 2.2 ns. This corresponds to the thermodynamics-driven segregation of the inner Cr cluster to the surface.

However, in the case for R = 60 Å in Fig. 7(b), $\varepsilon_{\mathrm{Cr}}$ is initially larger than $\varepsilon_{\mathrm{Fe}}$ and $\varepsilon_{\mathrm{Ni}}$, unlike the one in Fig. 7(a), due to the stochastic atomic distribution at 300 K. At all the temperatures, the deformation parameters are: $\varepsilon_{\mathrm{Cr}} > \varepsilon_{\mathrm{Ni}} > \varepsilon_{\mathrm{Fe}}$, which is consistent with the diffusion behavior in experiments, i.e., $D_{\mathrm{Cr}} > D_{\mathrm{Ni}} > D_{\mathrm{Fe}}$ [51,52]. It is expected that higher mobility results in a larger ε. Although the same is not observed for R = 40 Å, it eventually exhibits $\varepsilon_{\mathrm{Cr}} > \varepsilon_{\mathrm{Ni}} > \varepsilon_{\mathrm{Fe}}$ upon further heating. Near to T_{m}, there is a sharp increase in ε, and the relatively larger $\varepsilon_{\mathrm{Cr}}$ indicates the surface melting associated with severe Cr segregation. Given that the inner Cr clusters are broadly distributed (see the snapshot at T_2 = 1678 K in Fig. 7(b)), they might have insufficient driving force to coalesce in the interior. Contrarily, they would diffuse and aggregate to the surface to reduce the total surface energy, which is shown by the minor peaks of $\varepsilon_{\mathrm{Cr}}$ at 1754 and 1961 K for the additional net outward movement of Cr clusters.

It is evident that Cr segregation and aggregating occur concurrently at elevated temperatures. Therefore to gain a better insight into the Cr aggregation, the volumetric concentration of the Cr clusters at various temperatures was estimated for different radii and it is defined as

$$C_V = \frac{\sum_{i=1}^{n} V_i}{V_0} \tag{8}$$

where V_0 is the initial nanoparticle volume, n and V_i are the total number and individual volume of Cr aggregates, respectively. Here, the volume of the Cr aggregates can be calculated based on a surface construction algorithm [53] implemented in the Construct Surface Mesh Modifier in Ovito [54]. In this method, a probe sphere radius parameter is required and it is usually determined as the nearest neighbor

atom separation of the material of interest. The nearest neighbor distance between atoms is about 2.5 Å for the Fe-Ni-Cr nanoparticles. The variation of the volumetric concentration of Cr clusters as a function of temperature for the nanoparticles is shown in Fig. 8. Since T = 1000 K, the mobile Cr atoms diffuse and aggregate to the surface, and C_V gradually increases with the temperature. When the molten liquid-like layer proceeds from the surface to the core, the Cr clusters quickly form near the surface and exhibit a rapid growth mode. Moreover, it is also found that the growth rate of the Cr clusters increases with decreasing radius due to the larger surface atoms. After that, many inner Cr clusters develop upon the thermal effect until C_V approaches to a steady value of 14% to 16%, which is close to the total volume concentration of the Cr atoms (about 18%) in the Fe-Ni-Cr nanoparticles. If the atomic diffusivity time is sufficiently long, almost all the Cr would segregate and aggregate to the surface, and this is due to their relatively low surface energy and strong cohesive interactions.

3.4 Size-dependent melting point

In addition to atomic CSP values, the melting temperature of nanoparticles can also be identified by studying the variations in thermodynamic and structural properties such as potential energy and Lindemann index.

In this work, the temperature dependence of the average potential energy of the Fe-Ni-Cr nanoparticles with various radii is shown in Fig. 9. We can see that the atomic potential energy gradually increases with temperature, and then it suddenly rises at T_m indicating the occurrence of the surface melting. After that, the potential energy starts to decrease quickly before it further increases with the temperature. The sharp increase and decrease is due to a synergetic result of heat adsorption of melting and progressive Cr aggregation with T. However, this distinct hump in the potential energy has not been observed in other nanoparticle systems [16-20], which only exhibit a simple jump during melting transition from solid to liquid state. The energetically favored Cr segregation and aggregation decrease the surface energy, compromise the conformational entropy differences between the solid and transition states, and therefore lower the internal energy of the nanoparticles during melting. The temperature of the phase transition can be regarded as the one at which the potential energy starts to increase sharply. This gives rise to the melting temperatures T_m of 1599 and 1640 K for R = 40 and 60 Å respectively. In all the cases ($R \leq 70$ Å), the melting points are approaching towards the bulk melting temperature of

316L stainless steel (1693 K) [55,56] and the depression effect is intensified at smaller particles due to increasing surface atoms.

In a system containing *N* atoms, the Lindemann index δ is defined as the relative root-mean-square bond-length fluctuation and it is computed as [57-59]

$$\delta = \frac{1}{N(N-1)} \sum_{i \neq j} \sqrt{\langle r_{ij}^2 \rangle_t - \langle r_{ij} \rangle_t^2} / \langle r_{ij} \rangle_t \tag{9}$$

where r_{ij} is the distance between atoms *i* and *j*. The Lindemann index is useful in understanding the thermal properties and melting behaviors of nanoparticles. Fig. 10 shows the temperature dependence of the Lindemann index of the Fe-Ni-Cr nanoparticles for various radii during heating. It is clearly seen that the Lindemann index increases slowly at low temperatures because of the smooth increase in atomic kinetic energy with the temperature. The value of δ in this stage is very small since the atoms undergo small amplitude vibrations about their original lattice sites with the root-mean-square deviations in the bond lengths being less than 3%. During melting transition, the atoms gain some translational freedom, and this index increases rapidly by as much as a factor of 3. Especially, the melting point T_m can be obtained by the sharp increase in δ. At the temperature corresponding to the abrupt change, most of the atoms exhibit large amplitude diffusion in transition state, considered as melting of nanoparticle [57-59]. The melting points estimated from Fig. 10 are consistent with those shown in Fig. 9, and they are summarized in Table 1.

It is known that, when the radius is below a critical value, the melting point of the nanoparticle decreases with decreasing radius. Although there is no linear function between the melting point and radius, it varies linearly with the reciprocal of the radius [10,60,61]. This linear relationship is also observed for the Fe-Ni-Cr nanoparticles in our simulations, as shown in Fig. 11.

The lowering of the melting point with respect to the reciprocal of the particle radius can be related to the Nanda fitting equation which is computed as [10,43]

$$\frac{T_m(r)}{T_{m,bulk}} = 1 - \frac{6v_0\gamma}{\alpha T_{m,bulk} d} = 1 - \frac{\beta}{2R} \tag{10}$$

with

$$\beta = \frac{6v_0\gamma}{\alpha T_{m,bulk}} \tag{11}$$

where T_m and $T_{m,bulk}$ are the melting temperatures for nanoparticles and corresponding bulk phase respectively, R is the particle radius, v_0 is the atomic volume, γ is the coefficient of surface energy, α is a content with a value of 0.00055424 eV/K for FCC crystal structure, and β is a self-determined parameter (see Eq. (11)) of the material of interest. The atomic volume deduced from the molar volume is 0.0080, 0.0081 and 0.0082 nm^3 for Fe, Ni and Cr, and the corresponding coefficients of surface energy are 2206, 2104, and 2031 mJ/m^2 [10]. Considering that the two parameters for the alloy are unknown, we use a simple geometric mixing law [46] to predict the effective v_0 and γ for the Fe-Ni-Cr nanoparticles, that is, v_0 = 0.0080 nm^3 and γ = 2160 mJ/m^2. As a result, the value of β_{Nanda} is estimated to be around 0.697 using Eq. (11), in contrast to β_{MD} (0.548) as observed in the MD simulations. Compared with all the calculated values in Fig. 11, it is found that our simulated melting points of the nanoparticles are marginally higher than those of the theoretical model. This discrepancy could be due to two reasons. Firstly, the heating rate of the simulation process is much higher than that of the experiment, and the nanoparticles could have insufficient time to melt under rapid heating, resulting in a larger T_m. Secondly, the Nanda equation derived from the liquid-drop model may be inadequate to describe the size-dependent melting behaviors of the alloy nanoparticles, as described in ref. [60].

4 Conclusions

In this work, we performed MD simulations to investigate the melting characteristics and behaviors of the Fe-Ni-Cr nanoparticles. Their structural evolution and phase transition were characterized during heating in terms of CSP distribution, RDF, shell-based self-diffusion coefficients, density profiles, and radial deformation parameters. Through the calculations, it was found that the melting of the Fe-Ni-Cr nanoparticles begins from the surface and proceeds gradually toward the core, indicative of the LNG melting mode. During heating, progressive Cr segregation and aggregation with increasing temperature were also observed, and the anomalous “convex nano clusters” of Cr exhibit the maximum growth rate at phase transition from the solid to liquid state. The Cr segregation and aggregation is energetically favored due to the fact that the Cr atoms have less surface energy than Fe and Ni and possess stronger cohesive interactions with themselves. Moreover, the melting temperature of the nanoparticles at

various radii was identified by studying the variations of potential energy and Lindemann index. The size-dependent melting points of the nanoparticles were also compared with the Nanda equation. Although a smaller β was estimated in MD simulations, both calculations predict a linear relationship between the melting temperature and the inverse of the particle radius. The findings in this work are of particular value to provide the atomic scale understanding of the melting mechanisms, distinct surface segregation and aggregation of ternary Fe-Ni-Cr nanoparticles.

Acknowledgements

This work is supported by the National Natural Science Foundation of China (51603160), the Excellent Dissertation Cultivation Funds of Wuhan University of Technology (2017-YS-011), and Fundamental Research Funds for the Central Universities (WUT:172401008). C. H. Wong, Y. M. Zhang and C. J. W. Lim are supported by the National Research Foundation, Prime Minister's Office, Singapore under the National Additive Manufacturing Innovation Cluster (NAMIC) programme (RCA-17/357) and under the Medium-Sized Centre funding scheme.

References

[1] L.H. Lu, J.H. Liu, Y. Hu, Y.W. Zhang, W. Chen, Graphene-stabilized silver nanoparticle electrochemical electrode for actuator design, Adv. Mater. 25 (2013) 1270-1274.

[2] S. Son, Y.J. Jang, J. Park, H.B. Na, H.M. Park, H.J. Yun, J. Lee, T. Hyeon, Designed synthesis of atom-economical Pd/Ni bimetallic nanoparticle-based catalysts for sonogashira coupling reactions, J. Am. Chem. Soc. 126 (2004) 5026-5027.

[3] L. Kyeong-Seok, M.A. El-Sayed, Gold and silver nanoparticles in sensing and imaging: Sensitivity of plasmon response to size, shape, and metal composition, J. Phys. Chem. B 110 (2006) 19220-19225.

[4] J. Zhang, R.D.K. Misra, Magnetic drug-targeting carrier encapsulated with thermosensitive smart polymer: Core–shell nanoparticle carrier and drug release response, Acta Biomater. 3 (2007) 838-850.

[5] B. Jürgens, C. Kübel, C. Schulz, T. Nowitzki, V. Zielasek, J. Biener, M.M. Biener, A.V. Hamza, M. Bäumer, New gold and silver-gold catalysts in the shape of sponges and sieves, Gold Bull. 40 (2007) 142-149.

[6] W.H. De Jong, P.J.A. Borm, Drug delivery and nanoparticles: Applications and hazards, Int. J. Nanomed. 3 (2008) 133-149.

[7] C. Zhu, X.M. Cheng, Y.Y. Li, B.M. Tao, Influence of heat treatment on solidus temperature of NaNO3-KNO3 molten salt, Sol. Energy 118 (2015) 303-312.

[8] Y. Huang, X.M. Cheng, Y.Y. Li, G.M. Yu, K. Xu, G. Li, Effect of of in-situ synthesized nano-MgO on thermal properties of NaNO3-KNO3, Sol. Energy 160 (2018) 208-215.

[9] C.H. Cui, L. Gan, M. Heggen, S. Rudi, P. Strasser, Compositional segregation in shaped Pt alloy nanoparticles and their structural behaviour during electrocatalysis, Nature Mater. 12 (2013) 765.

[10] K.K. Nanda, S.N. Sahu, S.N. Behera, Liquid-drop model for the size-dependent melting of low-dimensional systems, Phys. Rev. A 66 (2002) 013208.

[11] Q. Jiang, X.H. Zhou, M. Zhao, Nucleation temperature of elements, J. Chem. Phys. 117 (2002) 10269-10273.

[12] J. Sun, S.L. Simon, The melting behavior of aluminum nanoparticles, Thermochim. Acta 463 (2007) 32-40.

[13] A. Safaei, M.A. Shandiz, S. Sanjabi, Z.H. Barber, Modeling the melting temperature of nanoparticles by an analytical approach, J. Phys. Chem. C 112 (2008) 99-105.

[14] R.A. Yetter, G.A. Risha, S.F. Son, Metal particle combustion and nanotechnology, Proc. Combust. Inst. 32 (2009) 1819-1838.

[15] H. Li, P.D. Han, X.B. Zhang, M. Li, Size-dependent melting point of nanoparticles based on bond number calculation, Mater. Chem. Phys. 137 (2013) 1007-1011.

[16] L.J. Lewis, P. Jensen, J.L. Barrat, Melting, freezing, and coalescence of gold nanoclusters, Phys. Rev. B 56 (1997) 2248-2257.

[17] A. Aguado, J.M. Lopez, J.A. Alonso, M.J. Stott, Melting in large sodium clusters: An orbital-free molecular dynamics study, J. Phys. Chem. B 105 (2001) 2386-2392.

[18] S.P. Huang, P.B. Balbuena, Melting of bimetallic Cu-Ni nanoclusters, J. Phys. Chem. B 106 (2002) 7225-7236.

[19] S. Sankaranarayanan, V.R. Bhethanabotla, B. Joseph, Molecular dynamics simulation study of the melting of Pd-Pt nanoclusters, Phys. Rev. B 71 (2005) 195415.

[20] S.J. Mejia-Rosales, C. Fernandez-Navarro, E. Perez-Tijerina, J.M. Montejano-Carrizales, M. Jose-Yacaman, Two-stage melting of Au-Pd nanoparticles, J. Phys. Chem. B 110 (2006) 12884-12889.

[21] J.L. Rodriguez-Lopez, J.M. Montejano-Carrizales, M. Jose-Yacaman, Molecular dynamics study of bimetallic nanoparticles: the case of AuxCuy alloy clusters, Appl. Surf. Sci. 219 (2003) 56-63.

[22] T. Shen, W.J. Meng, Y.Q. Wu, X.G. Lu, Size dependence and phase transition during melting of fcc-Fe nanoparticles: A molecular dynamics simulation, Appl. Surf. Sci. 277 (2013) 7-14.

[23] L.J. Meng, X.Y. Peng, K.W. Zhang, C. Tang, J.X. Zhong, Structural phase transitions of FeCo and FeNi nanoparticles: A molecular dynamics study, J. Appl. Phys. 111 (2012) 024303.

[24] J.M. Ortiz-Roldan, A. Rabdel Ruiz-Salvador, S. Calero, F. Montero-Chacón, E. García-Pérez, J. Segurado, I. Martin-Bragado, S. Hamad, Thermostructural behaviour of Ni–Cr materials: Modelling of bulk and nanoparticle systems, Phys. Chem. Chem. Phys. 17 (2015) 15912-15920.

[25] J. Kell, J.R. Tyrer, R.L. Higginson, R.C. Thomson, Microstructural characterization of autogenous laser welds on 316L stainless steel using EBSD and EDS, J. Microsc. 217 (2005) 167-173.

[26] M. Bohra, P. Grammatikopoulos, R.E. Diaz, V. Singh, J.L. Zhao, J.F. Bobo, A. Kuronen, F. Djurabekova, K. Nordlund, M. Sowwan, Surface segregation in Chromium-doped NiCr alloy nanoparticles and its effect on their magnetic behavior, Chem. Mater. 27 (2015) 3216-3225.

[27] G. Bonny, N. Castin, D. Terentyev, Interatomic potential for studying ageing under irradiation in stainless steels: the FeNiCr model alloy, Modell. Simul. Mater. Sci. Eng. 21 (2013) 085004.

[28] S. Pal, M. Meraj, Structural evaluation and deformation features of interface of joint between nano-crystalline Fe–Ni–Cr alloy and nano-crystalline Ni during creep process, Mater. Des. 108 (2016) 168-182.

[29] E. Sak-Saracino, H.M. Urbassek, The α↔γ transformation of an Fe1−xCrx alloy: A molecular-dynamics approach, Int. J. Mod. Phys. C 27 (2016) 1650124.

[30] C.J. Wu, B.J. Lee, X.P. Su, Modified embedded-atom interatomic potential for Fe-Ni, Cr-Ni and Fe-Cr-Ni systems, Calphad 57 (2017) 98-106.

[31] C.E. Pinedo, A.P. Tschiptschin, Low temperature plasma carburizing of AISI 316L austenitic stainless steel and AISI F51 duplex stainless steel, REM: R. Esc. Minas 66 (2013) 209-214.

[32] J.C. Jiang, E.I. Meletis, Microstructure of the nitride layer of AISI 316 stainless steel produced by intensified plasma assisted processing, J. Appl. Phys. 88 (2000) 4026-4031.

[33] J. Lu, L. Hultman, E. Holmström, K.H. Antonsson, M. Grehk, W. Li, L. Vitos, A. Golpayegani, Stacking fault energies in austenitic stainless steels, Adv. Mater. 111 (2016) 39-46.

[34] D. Bäuerle, Laser processing and chemistry, Springer, New York, 2011.

[35] R.R. Letfullin, T.F. George, G.C. Duree, B.M. Bollinger, Ultrashort laser pulse keating of nanoparticles: Comparison of theoretical approaches, Adv. Opt. Technol. 2008 (2008) 8.

[36] Y.S. Ma, X.Y. Chen, B. Liu, Experimental study of lubricant depletion in heat assisted magnetic recording over the lifetime of the drive, Tribol. Lett. 47 (2012) 175-182.

[37] B. Li, C.H. Wong, Q. Chen, Kinetics of lubricant desorption and decomposition under heat treatment: A molecular dynamics study, Soft Matter 9 (2013) 700-708.

[38] B. Li, C.H. Wong, Depletion kinetics of perfluoropolyether films with functional end groups using molecular dynamics simulation, Polymer 54 (2013) 6008-6018.

[39] X. Dai, H. Li, X. Lei, S. Shen, S. Wu, S. Liu, H. Du, Modeling of formation and breaking of lubricant bridge in the head–disk interface by molecular dynamic simulation, Mol. Simul. 44 (2018) 94-99.

[40] S. Plimpton, Fast parallel algorithms for short-range molecular-dynamics, J. Comput. Phys. 117 (1995) 1-19.

[41] C.L. Kelchner, S.J. Plimpton, J.C. Hamilton, Dislocation nucleation and defect structure during surface indentation, Phys. Rev. B 58 (1998) 11085-11088.

[42] P.R. Couchman, W.A. Jesser, Thermodynamic theory of size dependence of melting temperature

in metals, Nature 269 (1977) 481-483.

[43] K.K. Nanda, Size-dependent melting of nanoparticles: Hundred years of thermodynamic model, Pramana 72 (2009) 617-628.

[44] G.K. Goswami, K.K. Nanda, Thermodynamic models for the size-dependent melting of nanoparticles: Different Hypotheses, Curr. Nanosci. 8 (2012) 305-311.

[45] M. Hou, Solid-liquid and liquid-solid transitions in metal nanoparticles, Phys. Chem. Chem. Phys. 19 (2017) 5994-6005.

[46] T.T. Li, C. He, W.X. Zhang, M. Cheng, Structural and melting properties of Cu-Ni clusters: A simulation study, J. Alloys Compd. 752 (2018) 76-84.

[47] R. Jayaganthan, G.M. Chow, Thermodynamics of surface compositional segregation in Ni–Co nanoparticles, Mater. Sci. Eng. B 95 (2002) 116-123.

[48] L. Deng, W.Y. Hu, H.Q. Deng, S.F. Xiao, Surface segregation and structural features of bimetallic Au−Pt nanoparticles, J. Phys. Chem. C 114 (2010) 11026-11032.

[49] L.X. Peng, E. Ringe, R.P. Van Duyne, L.D. Marks, Segregation in bimetallic nanoparticles, Phys. Chem. Chem. Phys. 17 (2015) 27940-27951.

[50] M. Bohra, P. Grammatikopoulos, V. Singh, J.L. Zhao, E. Toulkeridou, S. Steinhauer, J. Kioseoglou, J.F. Bobo, K. Nordlund, F. Djurabekova, M. Sowwan, Tuning the onset of ferromagnetism in heterogeneous bimetallic nanoparticles by gas phase doping, Phys. Rev. Mater. 1 (2017) 066001.

[51] B. Million, J. Růžičková, J. Vřešťál, Diffusion in Fe-Ni-Cr alloys with an FCC lattice, Mater. Sci. Eng. 72 (1985) 85-100.

[52] A.F. Smith, G.B. Gibbs, The volume and grain-boundary diffusion of Iron in 20 Cr/25 Ni/Nb stainless steel, Met. Sci. J. 2 (1968) 47-50.

[53] A. Stukowski, Computational analysis methods in atomistic modeling of crystals, J. Miner. Met. Mater. Soc. 66 (2014) 399-407.

[54] S. Alexander, Visualization and analysis of atomistic simulation data with OVITO–the Open Visualization Tool, Modell. Simul. Mater. Sci. Eng. 18 (2010) 015012.

[55] Z. Chen, Joint formation mechanism and strength in resistance microwelding of 316L stainless steel to Pt wire, J. Mater. Sci. 42 (2007) 5756-5765.

[56] T. Jagadeesha, T.J.S. Jothi, Studies on the influence of process parameters on the AISI 316L resistance spot-welded specimens, Int. J. Adv. Manuf. Tech. 93 (2017) 73-88.

[57] G. Chen, P. Zhang, H.W. Liu, Analysis of Pd-Ni nanobelts melting process using molecular dynamics simulation, J. Nanomater. 2013 (2013) 486527.

[58] B. Fu, L. Chen, F.F. Wang, Y.Q. Xie, X. Ye, Melting of icosahedral nickel clusters under hydrostatic pressure, J. Comput. Chem. 35 (2014) 2231-2238.

[59] Y. Engelmann, A. Bogaerts, E.C. Neyts, Thermodynamics at the nanoscale: Phase diagrams of nickel–carbon nanoclusters and equilibrium constants for phase transitions, Nanoscale 6 (2014) 11981-11987.

[60] W.H. Qi, M.P. Wang, Size and shape dependent melting temperature of metallic nanoparticles, Mater. Chem. Phys. 88 (2004) 280-284.

[61] U. Domekeli, S. Sengul, M. Celtek, C. Canan, The melting mechanism in binary Pd0.25Ni0.75 nanoparticles: Molecular dynamics simulations, Philos. Mag. 98 (2018) 371-387.

Table 1 Number of atoms N, particle radius R, melting temperature T_m, and the melting upper limit point T_{me} for the Fe-Ni-Cr nanoparticles obtained from MD simulations. The bulk melting temperature from the experiment is also shown as a comparison.

N	R (Å)	T_m (K)	T_{me} (K)
369	10	1200	1301
2899	20	1470	1561
9909	30	1557	1603
23455	40	1599	1638
45995	50	1623	1653
79213	60	1640	1672
125879	70	1645	1682
187945	80	1652	1690
Bulk crystal		1693[a]	

[a] Data for 316L stainless steel from refs. [55,56]

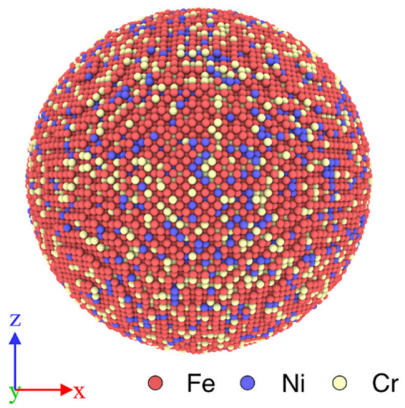

Fig. 1 Atomic distribution of a typical equilibrated Fe-Ni-Cr alloy nanoparticle of R = 60 Å at T = 300 K.

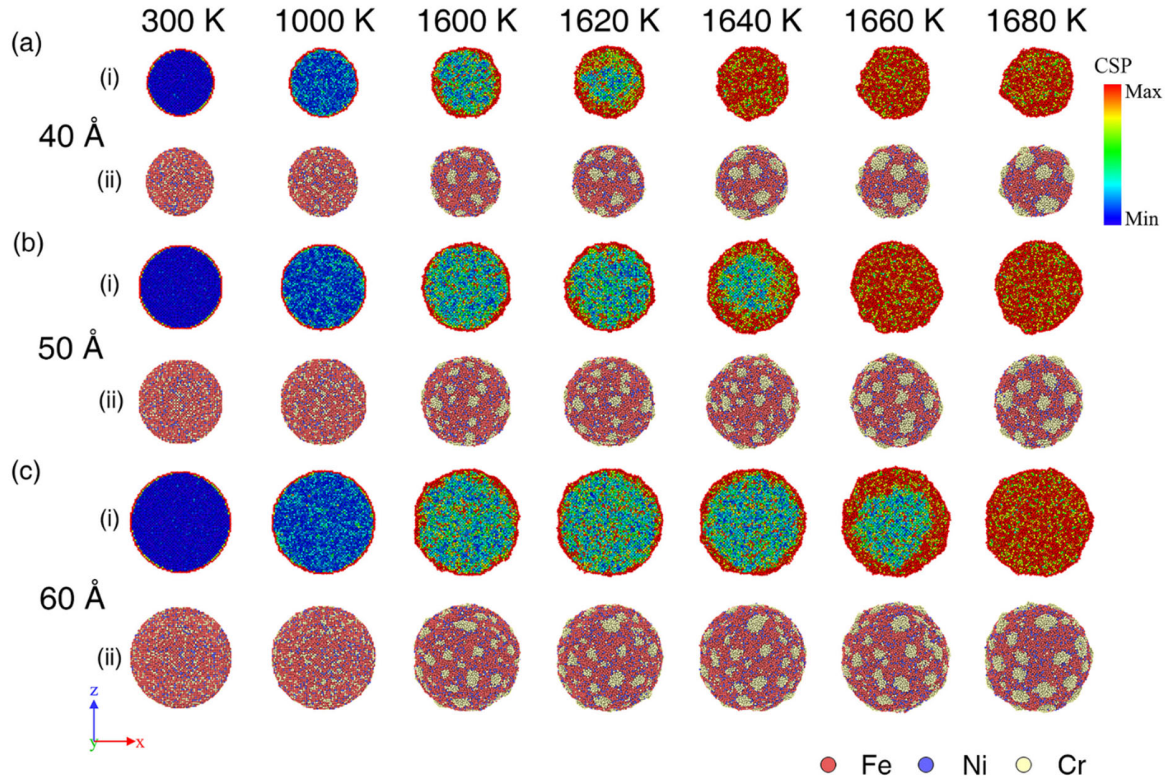

Fig. 2 Snapshots of the Fe-Ni-Cr nanoparticles of (a) R = 40 Å, (b) R = 50 Å and (c) R = 60 Å at different temperatures: (i) cross-sectional view of the atomic CSP and (ii) atomic distribution. In the color bar, blue represents a perfect FCC lattice and red indicates complete amorphization.

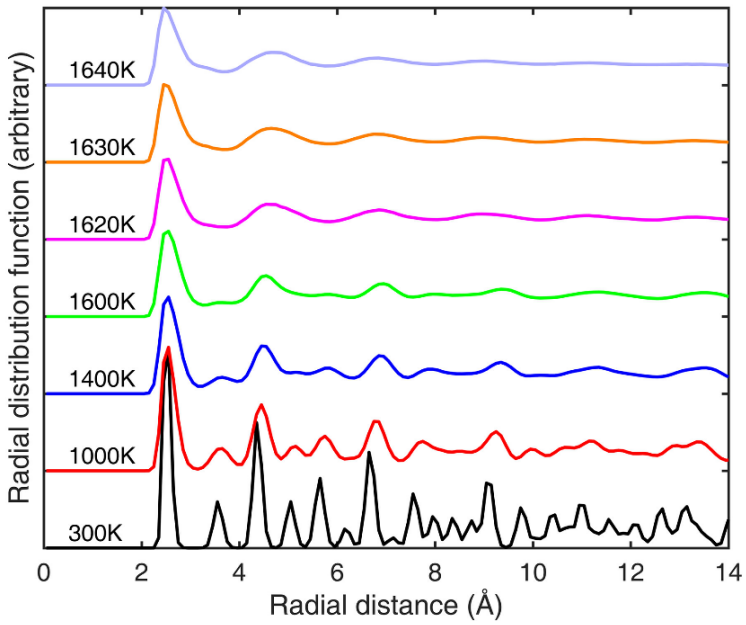

(a)

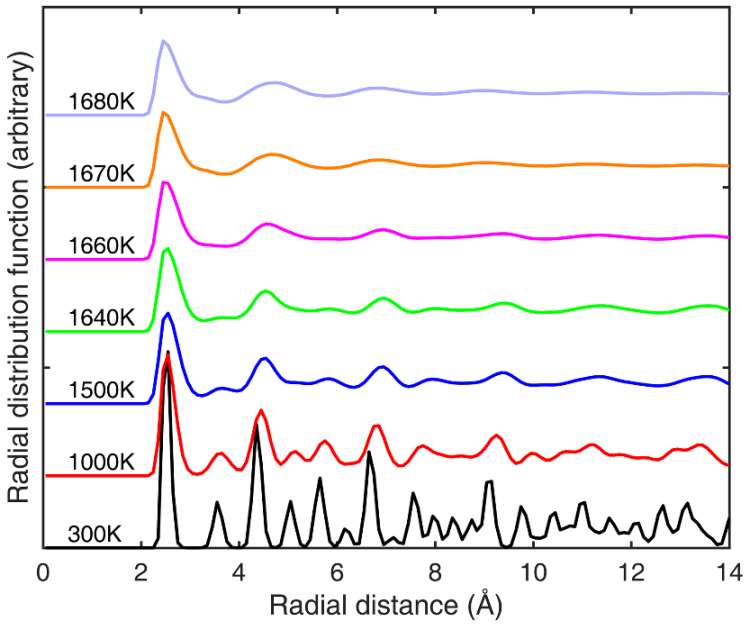

(b)

Fig. 3 Radial distribution function (RDF) profiles of Fe-Ni-Cr nanoparticles of (a) R = 40 Å and (b) R = 60 Å at different temperatures.

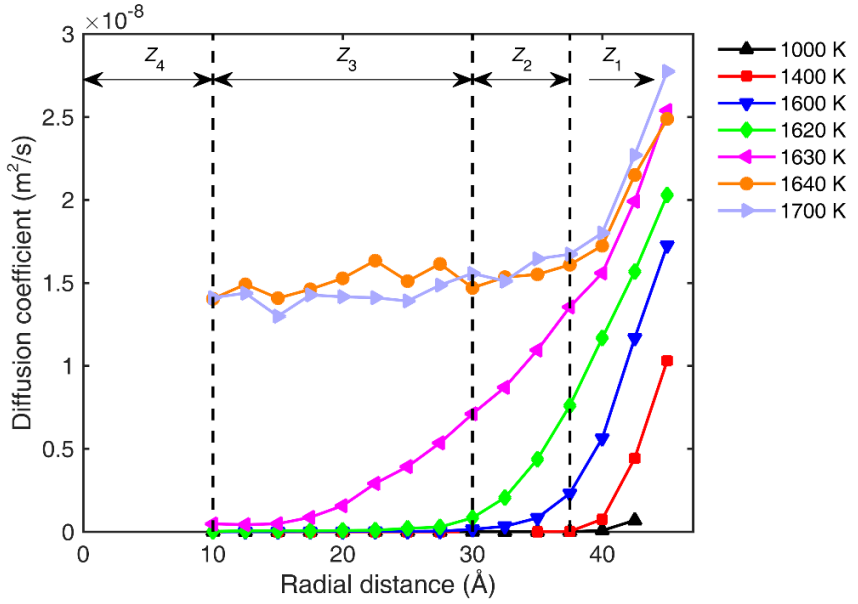

(a)

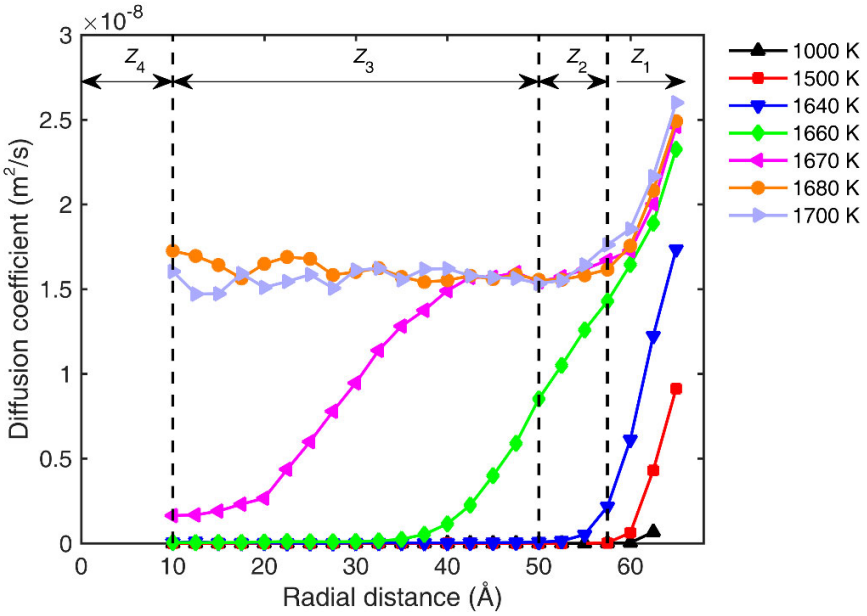

(b)

Fig. 4 Shell-based self-diffusion coefficient D of Fe-Ni-Cr nanoparticles of (a) R = 40 Å and (b) R = 60 Å at different temperatures.

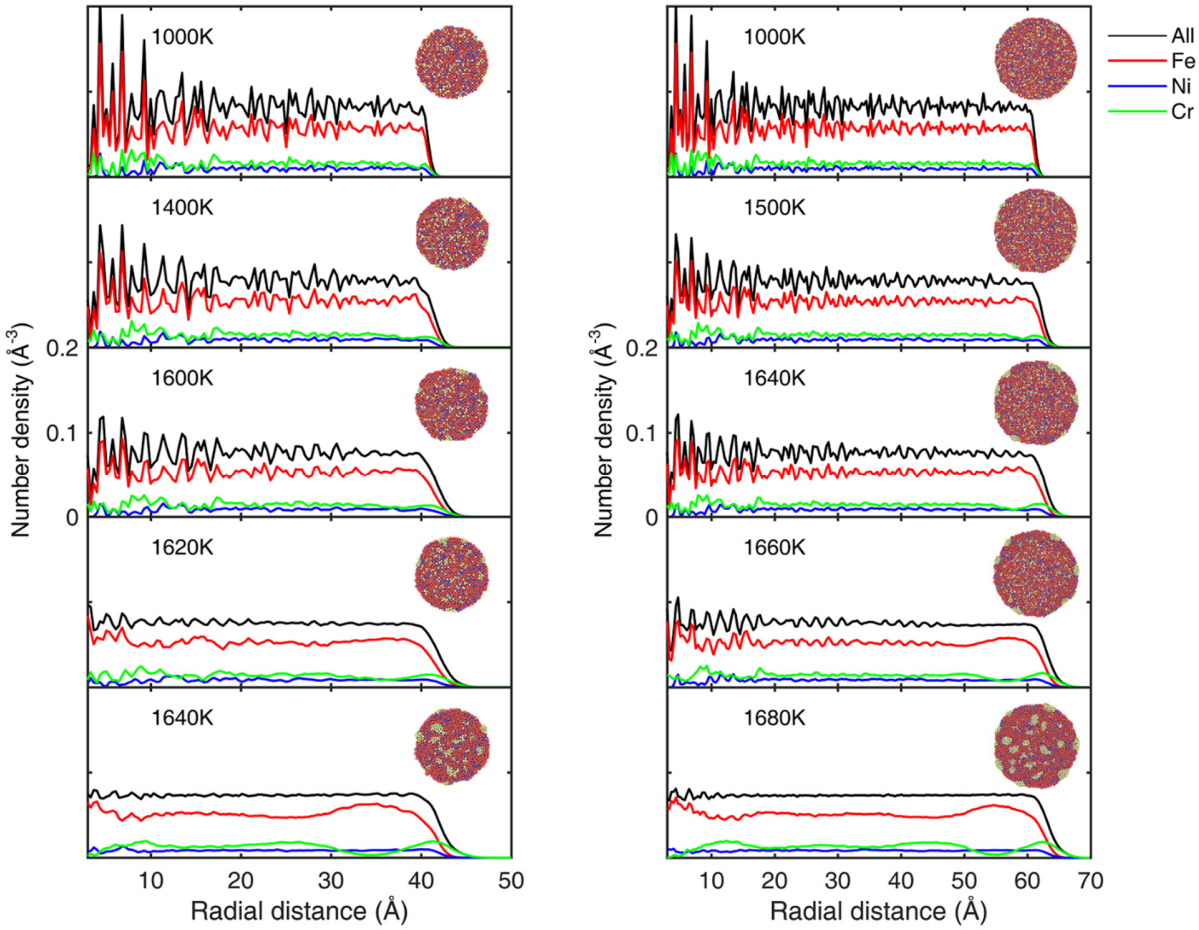

(a) (b)

Fig. 5 Total and partial density profiles of Fe-Ni-Cr nanoparticles of (a) R = 40 Å and (b) R = 60 Å at different temperatures. The inset is the corresponding cross-sectional view of the atomic distribution.

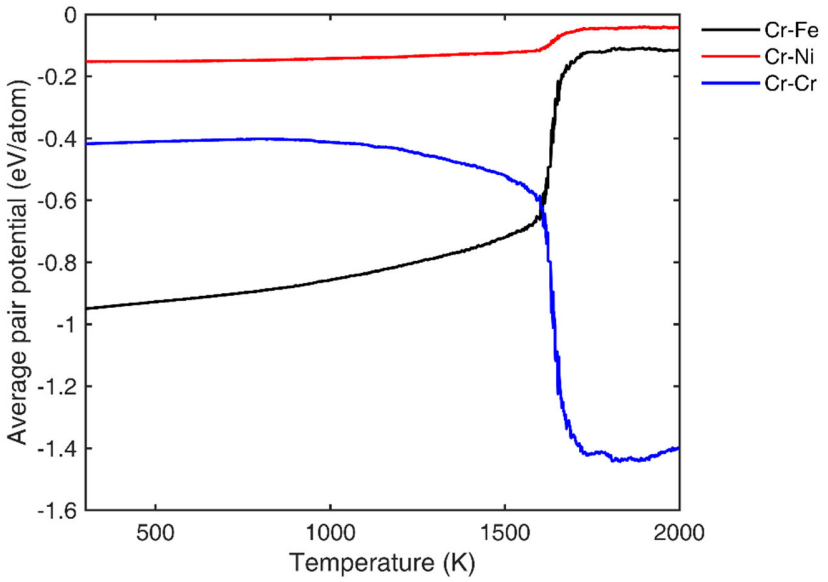

(a)

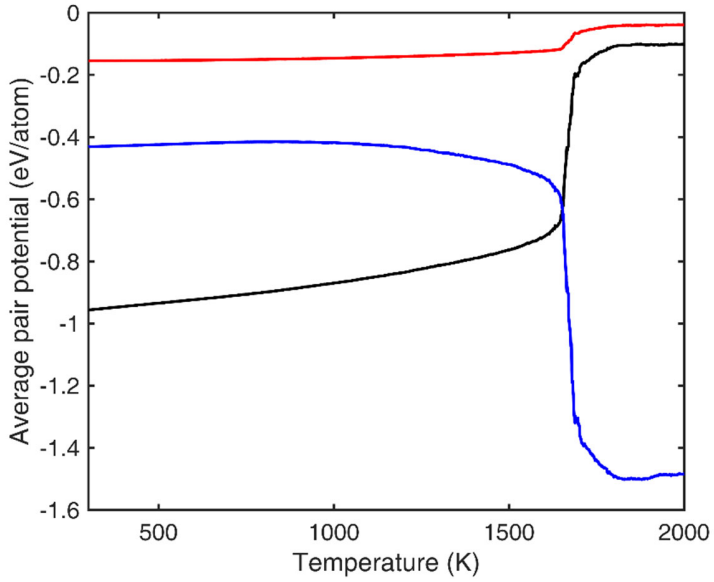

(b)

Fig. 6 The average pair interaction as a function of temperature for Fe-Ni-Cr nanoparticles of (a) R = 40 Å and (b) R = 60 Å.

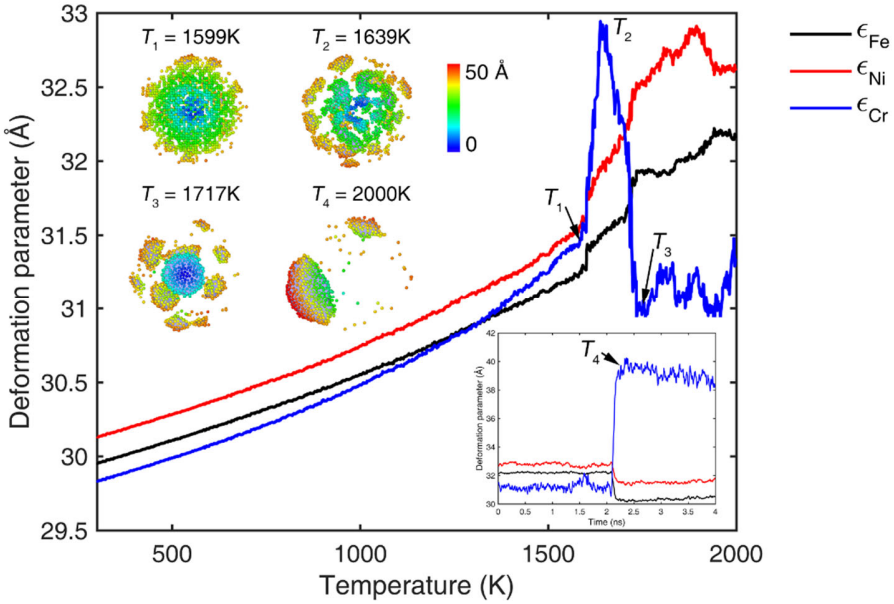

(a)

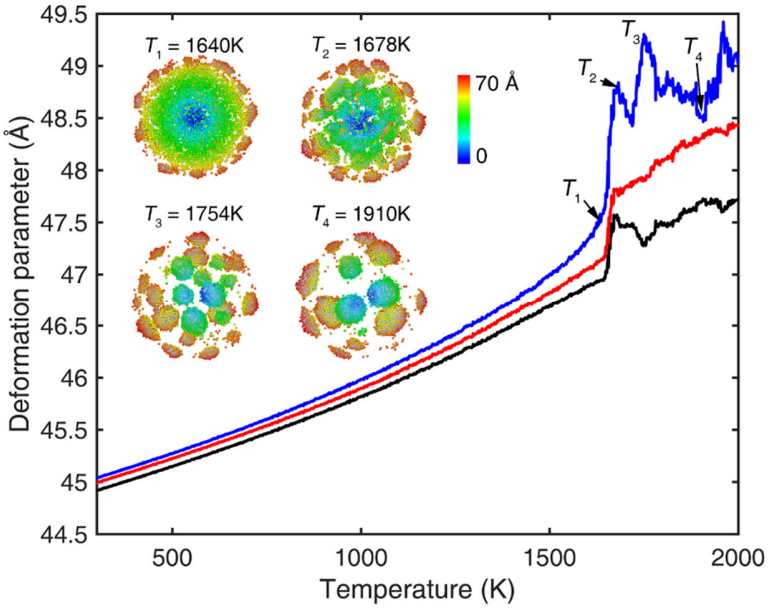

(b)

Fig. 7 The radial deformation parameters as functions of temperature for Fe-Ni-Cr nanoparticles of (a) R = 40 Å and (b) R = 60 Å. The color bar in the snapshots of the Cr atom distribution indicates the radial distance from the nanoparticle center. In the inset of Fig. 7(a), the deformation parameters of the nanoparticle with R = 40 Å at T= 2000 K for another 4 ns are calculated for better clarity.

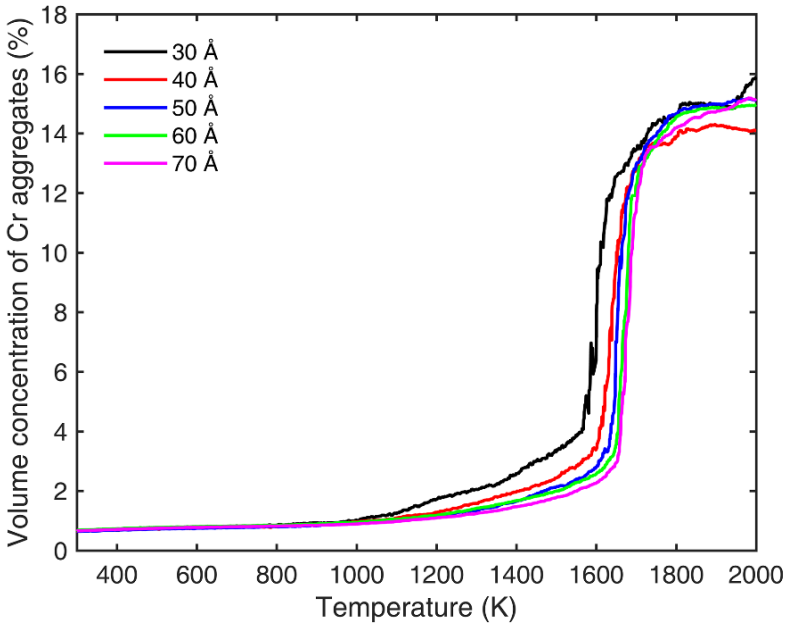

Fig. 8 The volume concentration of Cr aggregates as a function of temperature for various Fe-Ni-Cr nanoparticle radii.

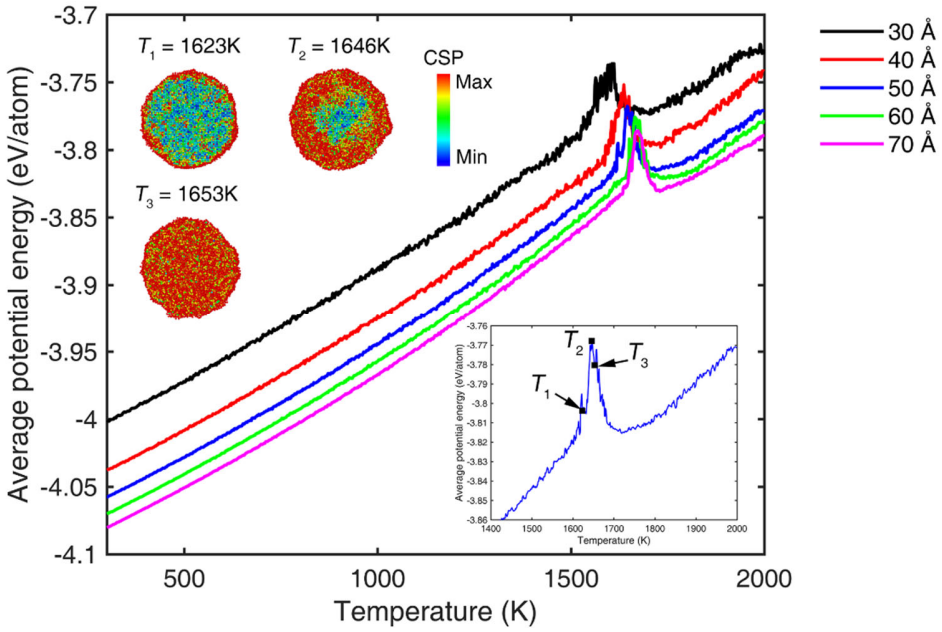

Fig. 9 The average potential energy as a function of temperature for various Fe-Ni-Cr nanoparticle radii. The enlarged potential energy curve and corresponding CSP distribution during heating for the nanoparticle with R = 50 Å are shown in the inset for better clarity.

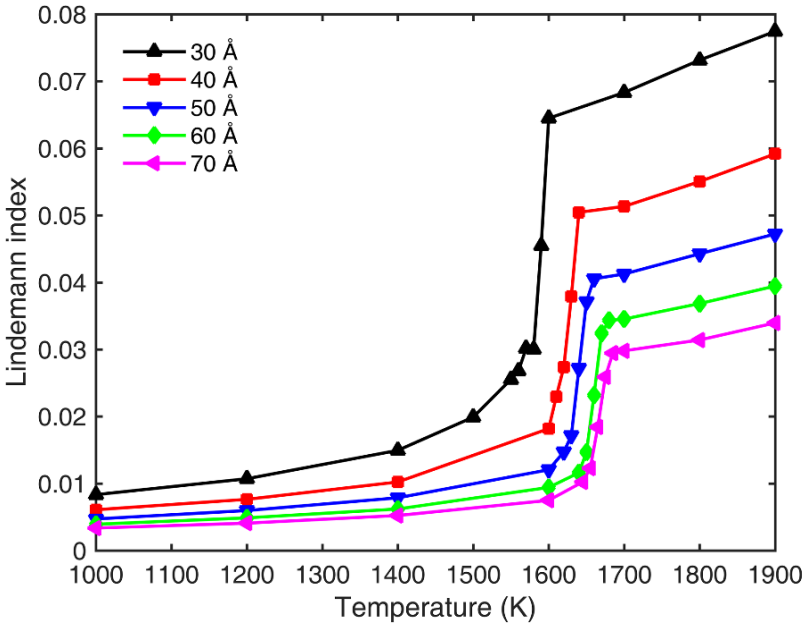

Fig. 10 The Lindemann index as a function of temperature for various Fe-Ni-Cr nanoparticle radii.

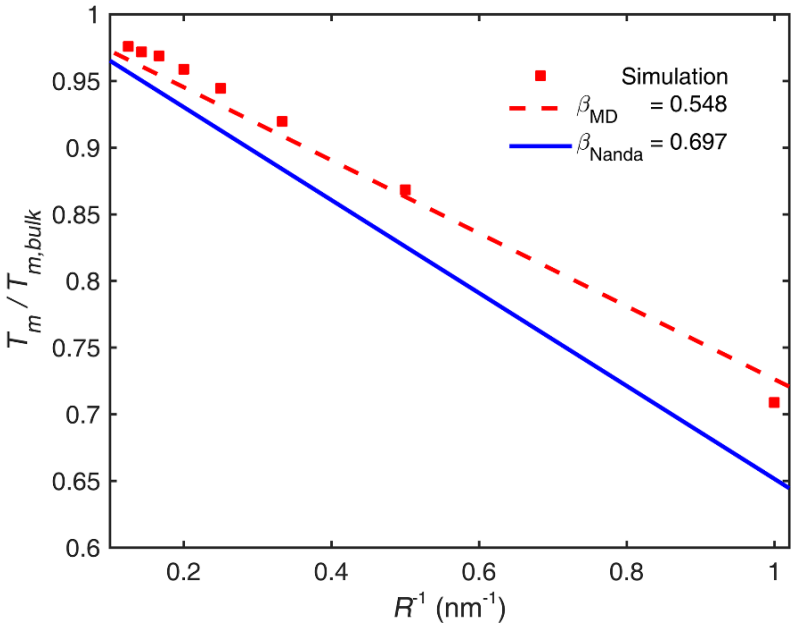

Fig. 11 Melting point *versus* the reciprocal of the particle radius for Fe-Ni-Cr nanoparticles. The dash line is the fitted curve for the MD simulation results, while the solid line is directly drawn using the effective v_0 and γ according to Eq. (11).

Atomic simulation of melting and surface segregation of ternary Fe-Ni-Cr nanoparticles

X. Zhang[a,b], B. Li[a,b,], H.X. Liu[b,c], G.H. Zhao[b,d], Q.L. Yang[a], X.M. Cheng[a], C.H. Wong[e,*], Y.M. Zhang[e], and C.W.J. Lim[e]*

[a] School of Materials Science and Engineering, Wuhan University of Technology, Wuhan 430070, China

[b] Research Center for Materials Genome Engineering, Wuhan University of Technology, Wuhan 430070, China

[c] International School of Materials Science and Engineering, Wuhan University of Technology, Wuhan 430070, China

[d] School of Computer Science and Technology, Wuhan University of Technology, Wuhan 430070, China

[e] Singapore Centre for 3D Printing, School of Mechanical and Aerospace Engineering, Nanyang Technological University, 50 Nanyang Avenue, Singapore 639798, Singapore

[*]Corresponding authors. E-mail: libei@whut.edu.cn, CHWong@ntu.edu.sg

Table S1 Comparison of lattice parameter and stacking fault energy for different bulk Fe-Ni-Cr alloys at T = 300 K between MD simulations and experiments.

	Composition, wt.%		Lattice parameter	Stacking fault energy
	Cr	Ni	(Å)	(mJ/m^2)
MD	19.17	11.72	3.57	19.7
	17.37	14.51	3.59 [31]	
Exp.	18.00	8.00	3.59 [32]	
	18.97	11.45		21.52 [33]

The accuracy of the MD simulations depends substantially on the selection of the force field. To justify the validity of Bonny's EAM potential [27], we have compared the calculated and experimental measured properties such as the lattice parameter and stacking fault energy. It is shown in Table S1 that the MD results agree well with the experiments, illustrating the applicability of Bonny's EAM potential to our Fe-Ni-Cr alloy models.

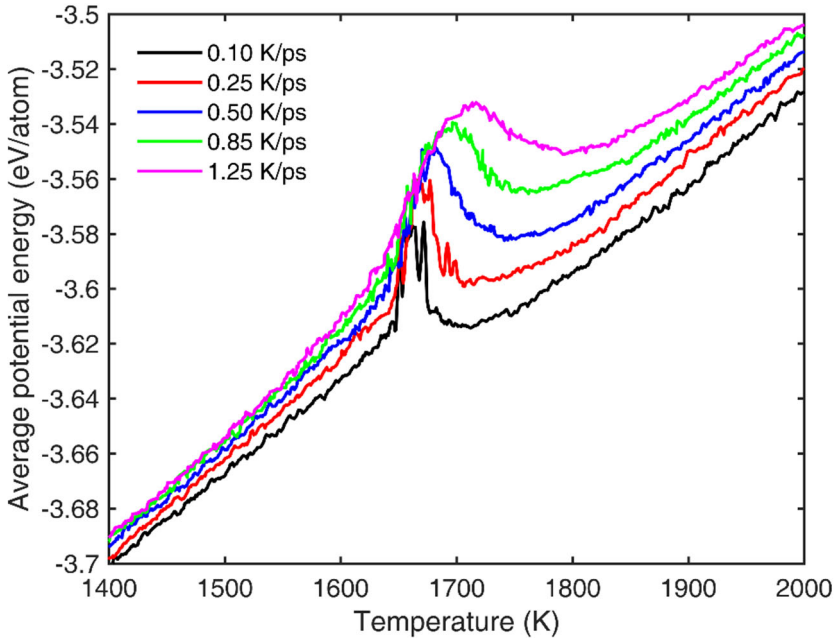

Fig. S1 The average potential energy as a function of temperature for various heating rates with R = 60 Å.

Table S2 Melting temperature T_m, and the melting upper limit point T_{me} for the Fe-Ni-Cr nanoparticles with R = 60 Å at various heating rates.

Heating rate β, (K/ps)	T_m (K)	T_{me} (K)
0.10	1642	1667
0.25	1640	1672
0.50	1640	1694
0.85	1634	1718
1.25	1618	1748

The effect of heating rate on the melting process of the nanoparticle with R = 60 Å is shown in Fig. S1. The corresponding melting temperature T_m, and the melting upper limit point T_{me} are also listed in Table S2. It is shown that the characteristic hump in the potential energy profiles becomes higher and wider at a larger heating rate β due to the thermal effect as well as the Cr segregation and aggregation during melting. More importantly, at $\beta > 0.25$ K/ps, T_m and T_{me} increase rapidly with increasing β, while they remain almost constant at $\beta \leq 0.25$ K/ps.

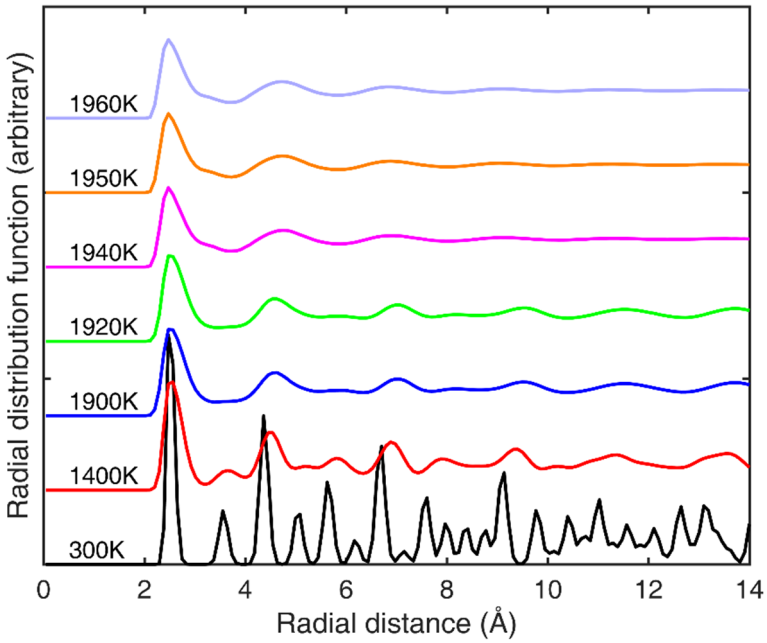

Fig. S2 Radial distribution function (RDF) profiles of the bulk Fe-Ni-Cr alloy at different temperatures.

Figure S2 shows the total RDFs as functions of the shell radius for the bulk Fe-Ni-Cr alloy at various temperatures, which is consistent with the observed features for the nanoparticles in Fig. 3.

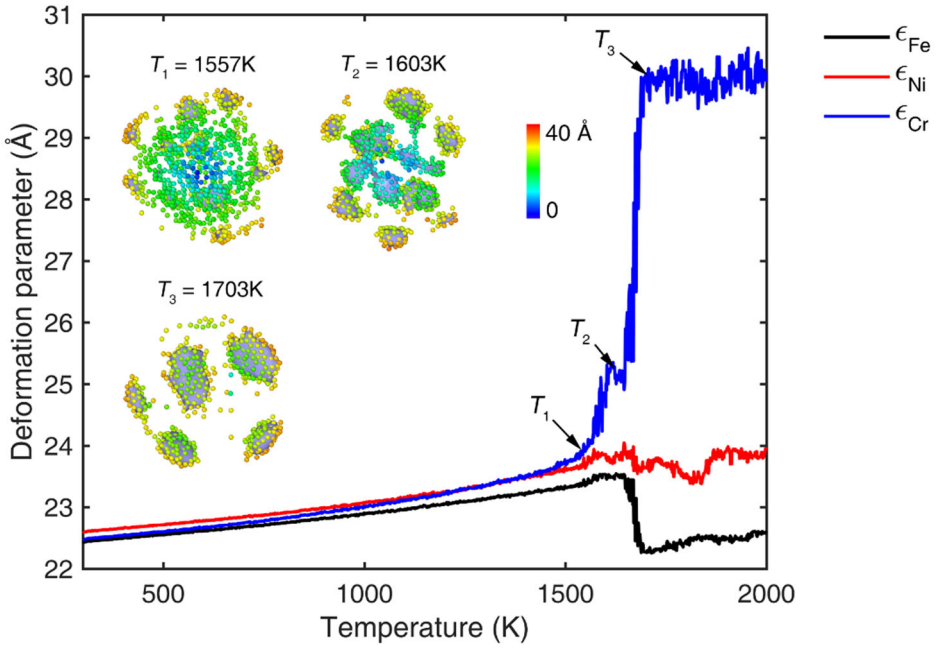
T_1 = 1557K
T_2 = 1603K
T_3 = 1703K
40 Å
0
T_1
T_2
T_3
ϵ_{Fe}
ϵ_{Ni}
ϵ_{Cr}
Deformation parameter (Å)
Temperature (K)

(a) R = 30 Å

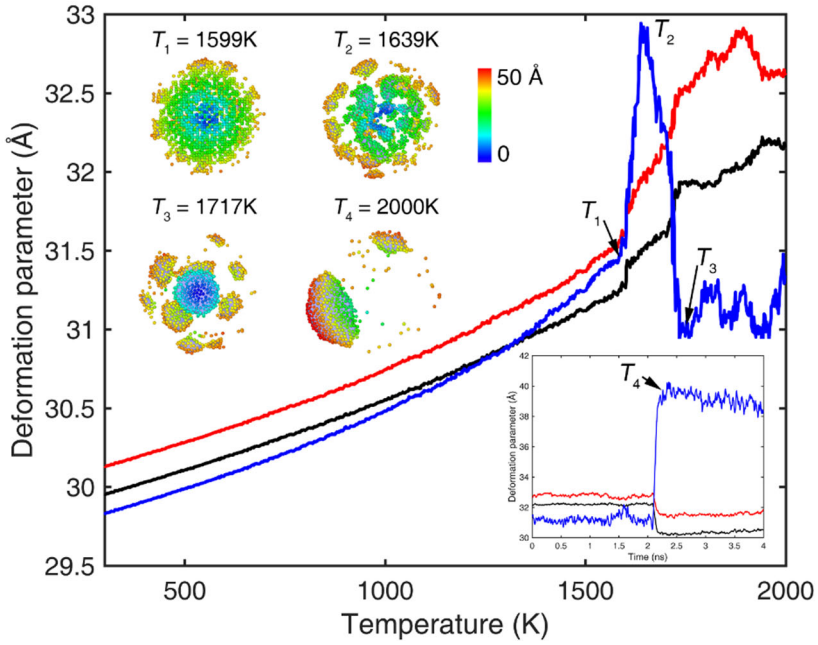
T_1 = 1599K
T_2 = 1639K
T_3 = 1717K
T_4 = 2000K
50 Å
0
T_1
T_2
T_3
T_4
Deformation parameter (Å)
Time (ns)
Deformation parameter (Å)
Temperature (K)

(b) R = 40 Å

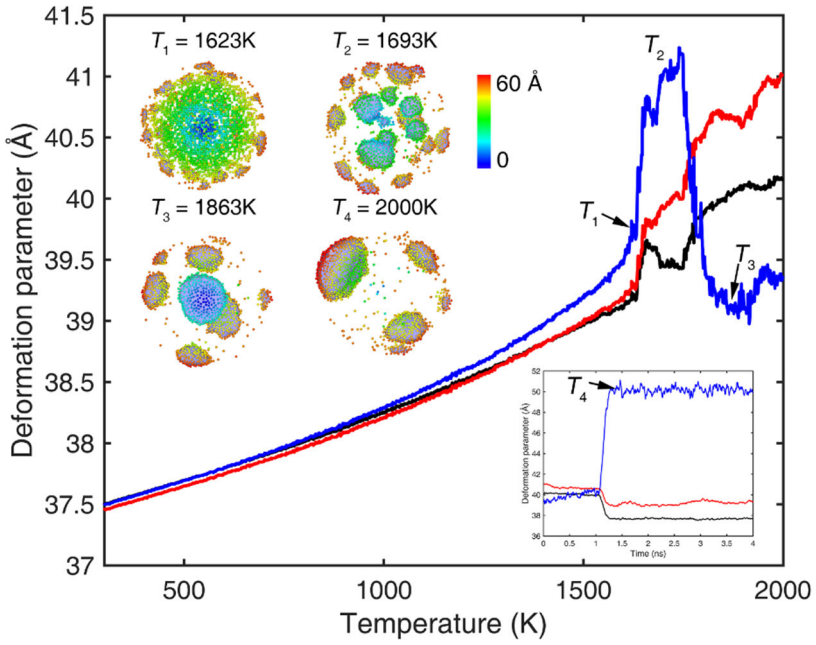

(c) R = 50 Å

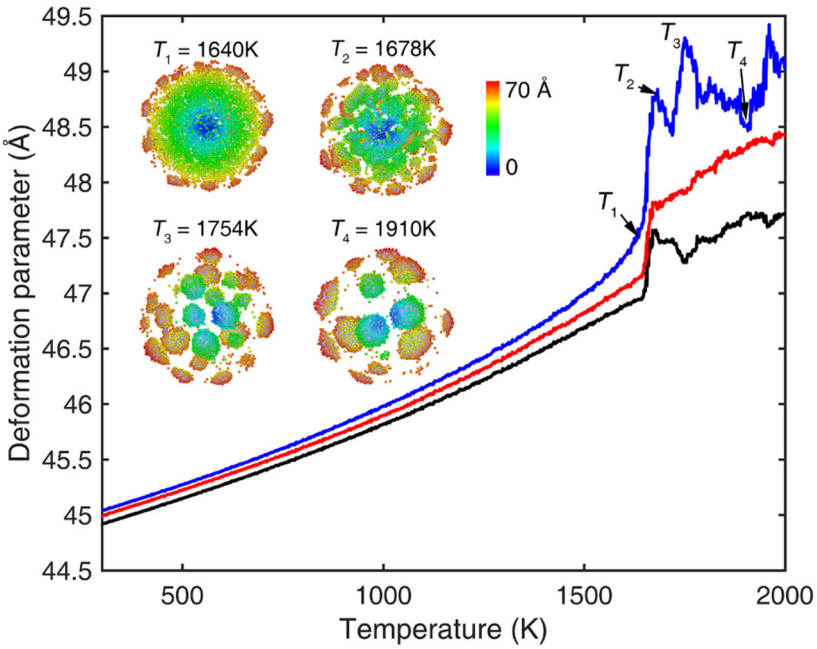

(d) R = 60 Å

Fig. S3 The radial deformation parameters as functions of temperature for Fe-Ni-Cr nanoparticles with various radii. The color bar in the snapshots of the Cr atom distribution indicates the radial distance from the nanoparticle center. In the insets of (b) and (c), the deformation parameters of the nanoparticles at T= 2000 K for another 4 ns are calculated for better clarity.

Figure S3 shows the radial deformation parameters as functions of temperature for the Fe-Ni-Cr nanoparticles at various radii. It is clearly shown that the deformation parameters present different sequences before melting. This is probably ascribing to the stochastic atomic distribution at 300 K. Then, ε_{Cr} rapidly increases as a result of Cr aggregation and segregation during melting, giving rise to $\varepsilon_{Cr} > \varepsilon_{Ni} > \varepsilon_{Fe}$. As the temperature continues to increase up to 2000 K, either an increase or a sharp decrease of ε_{Cr} occurs depending on the distribution of Cr aggregates in the interior. If the inner Cr nano clusters have insufficient driving force to coalesce in the interior, they would diffuse to the surface, causing a continuous increase in ε_{Cr}. Otherwise, they coalesce in the interior and ε_{Cr} decreases abruptly. However, for all the cases, it eventually exhibits $\varepsilon_{Cr} > \varepsilon_{Ni} > \varepsilon_{Fe}$ upon further heating, which is consistent with the diffusion behavior in experiments, i.e., $D_{Cr} > D_{Ni} > D_{Fe}$ [50,51].